ALMA Memo 372
An Amplitude Calibration Strategy for ALMA

R.Moreno IRAM, S.Guilloteau IRAM/ESO

May 10, 2002

Abstract

We propose an amplitude calibration strategy for ALMA which attempts to reach the 1 % precision for absolute calibration. Key points and major difficulties are identified. Polarization is ignored in this first step. We first review the properties of possible calibration sources. Planets and specially giant planets satellites are the preferred reference sources for flux calibration. Asteroids are too complex for such a purpose, but are useful as e.g. targets for relative pointing & focus determination. Stars are too weak. Quasars have to be used for various intermediate steps: bandpass, pointing, focus, and relative amplitude calibration.

The amplitude calibration precision may be divided into 3 major items: absolute flux scale, relative amplitude calibration (as function of time and antenna), and bandpass (dependence on frequency). Absolute amplitude depends on receiver gain and atmospheric opacity correction, and on pointing & focus control. The semi transparent vane is found to be 3 to 10 times less sensitive to atmospheric parameters than the dual-load calibration system. Accurate pointing & focus control can be done within reasonably short time (1 minute or so). Relative amplitude calibration can be checked to 1 % accuracy at mm wavelengths by observation of a nearby quasar, but integration time considerations prevents reaching better than about 3 % at submm wavelengths. Bandpass calibration, and specially the sideband ratio determination, is the longest calibration procedure. Within 3 minutes, this can be calibrated to 1 % at mm wavelengths, but only to 3 % at submm frequencies. Based on these considerations, we recommend 1) to further develop the semi-transparent vane system, 2) to keep the 1 % accuracy goal at mm wavelengths, 3) to relax the specification to 3 % in the submm domain, and 4) implement the coherent signal from the subreflector for bandpass calibration purpose.

1 Introduction

Calibration for ALMA is a major topic since it is an image quality limiting factor. The calibration problem has many facets:

- Phase calibration: phase errors will limit the image dynamic range

- Bandpass calibration: bandpass errors can affect the determination of velocity gradients, or line to continuum ratios.
- Relative amplitude calibration: relative errors will limit the dynamic range
- Absolute amplitude calibration: flux scale errors will limit the accuracy of the determination of physical parameters. Absolute amplitude calibration can play significant role in multi-wavelength analysis, or in the analysis of time variable phenomena
- Primary beam calibration: correction for the primary beam attenuation is required before scientific analysis.
- Polarization calibration: depending on the adopted observing scheme, amplitude and phase errors can influence the polarization measurements.

The ALMA Scientific Advisory Committee has set an ambitious goal of 1 % absolute calibration accuracy for ALMA. A relative amplitude accuracy of 1 % is needed for high dynamic range images (up to 10^4 or so). Reaching the same absolute accuracy is even more challenging. So far, "absolute" calibration is hardly ever performed. Instead, most arrays (even at cm wavelengths) rely on so-called **primary** amplitude calibrators, which have been measured in an absolute way once (or twice) and are assumed constant since then. For example, the VLA uses 3C48 and 3C286 as **primary** calibrators. At mm wavelengths, the primary calibrators are the solar system planets. However, they have not yet been measured or modeled with better than 5 % accuracy. At sub-mm wavelengths, the situation is even worse. With careful cross-checks, the IRAM interferometer currently achieves about 5 % accuracy at 3 mm, and 10 % at 1.3 mm.

Hence, the 1% goal for ALMA is very challenging: this is beyond the precision of the standard "chopper wheel" method [Yun et al. 1998], and has driven a number of studies of alternate calibration schemes [Bock et al. 1998], [Mangum 2000], [Plambeck 2000]. However, before facing up these serious issues, one should realize that calibration time may also become an important problem to reach such levels. In most cases, going from 5% to 1% typically implies 25 times longer calibration times.

This memo contains a study of the ALMA amplitude calibration scheme and the accuracy achieved at both mm and submm wavelengths for ALMA. A review of our knowledge on the calibration sources is presented in the first part. Based on the source flux at different wavelength and ALMA sensitivity, we compute the integration time needed, for a given accuracy, for each step in the calibration procedure: pointing, focus, bandpass, amplitude and phase, and absolute amplitude calibration. Finally, a global calibration scheme will be proposed.

2 The rules of the game

The main goal of calibration is to convert the raw correlation coefficient, as measured by the correlator, into an accurate physical quantity. Many factors influence this conversion:

1. The correlator quantization effects, which are fortunately stable and can be analytically derived
2. The receiver/electronic gain, which depends on frequency, and tuning parameters, and even on time if the receiver is not stable enough.
3. The antenna gain, which can change if the antenna is mis-pointed, ill-focused, or distorted by thermal effects. This antenna gain is not just a simple number, but the whole beam pattern may matter for sufficiently extended sources.
4. Atmospheric transparency, which must be accounted for properly.
5. Decorrelation coefficients, which result either from electronic phase noise, or from short (and medium) term atmospheric effects.

For a single-dish telescope, the last term plays no role. Proper focus and pointing control can guarantee a stable beam, provided the main dish deformation do not exceed some specified level. Atmospheric transparency correction becomes the most challenging problem, and it is usually performed with the receiver gain calibration, because the two problems do not easily separate. A direct **absolute** calibration relying on this atmospheric correction and on proper antenna beam modeling is quite possible. There is no stringent need to perform relative amplitude calibration to some reference flux standard.

For current mm interferometers, knowledge of the effective decorrelation factor is a serious issue. Hence, direct absolute calibration is not a standard practice at mm interferometers. Rather, they all proceed by doing a relative amplitude calibration based on regular observing of a nearby quasar, whose flux is bootstrapped to a reference flux standard (planet or other source). As a side effect, control of the pointing and focus if often relaxed, since first order effects for small sources are corrected by the relative amplitude calibration. Such a procedure is appropriate only for small sources.

Given the higher goals for ALMA, we propose to attempt a **direct absolute amplitude calibration as far as possible**. Proper calibration will require several steps:

1. Receiver tuning: sideband gain ratio
2. Delay and Bandpass measurement (amplitude and phase frequency dependence)
3. Atmospheric transparency calibration, also called atmospheric amplitude calibration
4. Pointing and Focus checks
5. Relative amplitude calibration
6. Phase calibration, and decorrelation estimates
7. Absolute flux scale determination

The goal of that paper is to determine how these actions could best be performed and what integration time they require. Once the time estimates are known, as well as their dependency on the required calibration accuracy, an optimized breakdown of the error budget can be given. In this paper, we use the following assumptions:

1. The basic phase calibration cycle uses two observing sky frequencies, one for observation $\nu_{\rm obs}$, one for calibration $\nu_{\rm cal}$.
2. An independent amplitude calibration cycle also exists, but only uses the observing sky frequency $\nu_{\rm obs}$.
3. An absolute calibration scale can ultimately be defined by using standard flux reference sources, if needed. To reach the required accuracy may require observing at two different frequencies, and use some a priori knowledge of the spectral index.

Small residual elevation dependence of the correlator output (due to improper atmospheric modeling) may be calibrated out in our scheme. This will be mentioned when relevant. We focus on **amplitude** calibration, and only mention **phase** calibration as far as integration times are concerned. In this approach, a typical observation session would be

```
 SIDEBAND(obs)
 DELAY(cal), DELAY(obs)
 FINE_BANDPASS(cal), COARSE_BANDPASS(obs)
    nf x (POINTING(cal), FOCUS(cal),
          na x (AMPLITUDE(obs),
                np (PHASE(cal), SOURCE(obs) )
               )
          )
) POINTING(cal), FOCUS(cal), FLUX(cal), FLUX(obs)
```

where `cal` and `obs` indicate the calibration frequency and observing frequency respectively. `POINTING` and `FOCUS` are assumed to be checked on a similar timescale in the above example, but this may not be true in all circumstances.

Astronomical Calibrators of various kinds are required in this approach (i.e. there is no independent absolute metrology). The next section describes the properties of relevant astronomical sources for this purpose.

3 Calibration Sources

3.1 Introduction

Planets and quasars are the main mm / submm calibration sources used in radioastronomy. With the higher sensitivity of ALMA, other calibration sources like satellites, asteroids and stars can also be used. We discuss in this section our knowledge of these sources on several points : source list / sky distribution, size, flux and spectral index, polarisation, variability / uncertainties. All these sources (except quasars) could be used as primary or secondary flux calibrators, depending of their relative size versus the synthesized beam (see Section 11). The quasars will not be used as flux calibrators, but as amplitude calibrators.

3.2 Planets and Satellites

Planets are intensively used as flux calibrators in the mm / submm range, because they have strong and reasonably well known fluxes. Although the absolute fluxes are not known with better than 5% accuracy, their time dependence is known much more accurately. Moreover, our good knowledge of the radiative processes involved and their size, allows independent modeling of the continuum brightness, which gives more confidence to the flux values of these primary calibrators in radioastronomy.

The mm/submm continuum of the Giant planets are modeled to about 4-10 % accuracy using a spherical radiative transfer code, and including collision induced absorption of the main compounds (H_2, He, CH_4) and ammonia far wing computation [de Pater and Massie 1985] [Lellouch et al. 1985] [Moreno, 1998]. Note that Uranus is the planet with the better observed/modeled mm/submm continuum, with uncertainties $< 5\,\%$. With similar atmospheric modeling, Titan's mm/submm continuum is known with the same level of accuracy [Paubert et al. 1984] [Gurwell 1995] [Hidayat 1997]. Furthermore, polarization at mm/submm wavelengths is negligible for the giant planets and Titan.

The planets and satellites which do not have thick atmosphere (Mars and Jovian's major satellites) can be modeled by a smooth isothermal dielectric sphere with dielectric constant (ϵ) depending of the soil properties. ϵ can be accurately measured at cm wavelength and knowing the frequency dependency, can be extrapolated to the mm/submm range. These modeling have reached an accuracy of about 5% in modeling the Mars mm/submm continuum [Rudy et al. 1987] [Rudy 1987], in agreement with absolute calibration measurements [Ulich 1981]. Near the planets limb, the flux is increasingly polarized (see Fresnel equations) but predictable. Since these planets / satellites will be partially resolved by ALMA, the polarized region will have a larger influence on the measured flux and should be also taken into account for a better accuracy. Extension of the Mars modeling to satellites and asteroids has been made [Mulheman and Berge 1991].

Planets have brightness temperatures between 70–200 K and their apparent sizes are between 2 and 45″. The major Jovian's satellites and Titan have angular diameter of $\sim 1''$ and brightness temperature between 70–100 K [Mulheman and Berge 1991] [Gurwell 1995]. The averaged satellites flux at 230 GHz is ~ 2.5 Jy.

The relatively large size of the planets and satellites make them easily resolved by mm interferometers, which complicates their use as primary flux calibrators. Standard practice is to bootstrap the flux of secondary calibrator (quasar or other small source) using total power measurements in single-dish mode. This is inherently less sensitive (by $2\sqrt{N_{\rm ant}}$ provided atmospheric noise and receiver gain variations and $1/f$ noise are negligible) than interferometry techniques. Modeling the continuum visibilities of the smallest planets (Uranus, Neptune and Mars) and satellites could allow to use them in interferometric mode at mm wavelengths. Self calibration techniques based on planet modeling have already been used to calibrate interferometric planetary observations [de Pater and Massie 1985] [Gurwell 1995] [Moreno et al. , 2001]. Therefore, interferometric observation of planets can be used to measure secondary calibrator fluxes, rather than having to rely on single-dish techniques to do so, at the expense of some sensitivity loss due to low visibilities on the longest baselines.

3.3 Asteroids

They are many classes of asteroids (Near, Main belt, Trojan, ...), most of them are located in the Main belt between 2–3 AU from the sun. At that distance the effective temperature due to the sun is $\sim$ 175 K. The most interesting asteroids size for our calibration purpose needs to be large enough to provide the strongest possible fluxes, but not to big ($<1''$), to remain unresolved as much as possible. The interesting size is $\sim$ $0.1''$corresponding to asteroids diameters of 200 km at a geocentric distance of 2.5 AU. The typical flux of these kind of asteroids is about 50 mJy at 230 GHz. There are about 60 asteroids included in this selection [Redman et al. 1995].

The radio wavelength observations of asteroids has been modeled in term of soil emissivity properties. The effective emissivity of the asteroids can vary between 0.5 to 0.9 in the mm/submm range [Redman et al. 1998]. Consequently, their brightness temperature are often lower than the effective temperature at a given heliocentric distance.

Due to the asteroid rotation, the light curve of big asteroids as Vesta (diameter of 520 km) shows flux variations of about 5% [Redman et al. 1992]. It is well known from radar observations that asteroids have very different shapes (e.g. include bone shape for 216 Kleopatra observed by [Ostro et al. 2000]). In addition, the average asteroid's rotation period is $\sim$ 0.5 days, which shows the difficulty to exactly predict the asteroid flux. Moreover, polarized emission from the asteroid edges will be a larger fraction than for the small planets or giant satellites.

Thus, asteroids will be difficult to use as primary calibrators. They could possibly play a role as secondary calibrators, specially at the highest observing frequencies where planets are difficult to use (too large) and quasars too faint. The flux prediction will need well calibrated flux measurement (i.e. versus planets) at different wavelengths to measure the asteroid mm/submm emissivity prior to their future use as secondary calibrators.

3.4 Stars

As indicated by [Yun et al. 1998], Giant and Supergiant stars can be used for flux calibration at submm wavelengths. They have submm flux $\sim$ 7 times stronger than nearby main sequence stars. [Yun et al. 1998] listed about 30 sources, with on average, a diameter of $0.005''$, a temperature of 4000 K and a flux at 690 GHz of 25 mJy. To first order, the photosphere of these stars, which are optically thick, radiate as a blackbody with spectral index of +2, and variability should be small. Extrapolation of the mm/submm flux from measurement at other frequencies may be possible. However, contribution from a stellar wind could perturb the spectral index, making an absolute flux prediction difficult.

Long period variable stars (e.g. Miras and semiregular variables) could be also used as flux calibrators as proposed by [Reid and Menten 1997] who observed 6 of these sources at cm wavelengths. Within a period of 100-1000 days, their flux can vary by $\pm$15% in mm/submm range, but periodically. The variations are mainly due to star pulsation which is also well modeled. The typical brightness temperature is about 1500 $\pm$ 500 K, and the angular sizes are $\leq 0.1''$. They have flux of $\sim$ 1 mJy at 22.4 GHz, which, extrapolated at 230 and 690 GHz, gives $\sim$ 100 and 1000 mJy, respectively. High precision, low

frequency measurements, combined with a known spectral index, could allow prediction of the flux at the highest frequencies, making these stars attractive flux calibrators in the submm domain. However, the spectral index ($\sim$ 1.7) of the emission may not be known with sufficient accuracy to allow accurate enough flux prediction.

Early type stars with stellar winds, like MWC 349 [Altenhoff et al 1994], could also play a special role. MWC 349 is quite strong (1.7 Jy at 230 GHz), and has a well defined spectral index of 0.6 over all the mm/submm range and even beyond, and is not variable. The spectral index is theoretically understood as resulting from a $1/r^2$ fully ionized gas distribution due to a stellar wind. This is thus a high brightness source (10^4 K), with a very small, frequency dependent, size ($\simeq 0.05''$). MWC 349 has been used as primary calibrator at the IRAM Plateau de Bure interferometer for several years. Similar objects in the southern sky could play the same role. ALMA could easily use stars which are 10 to 50 times weaker than MWC 349.

A detailed "a-priori" prediction of the flux density for these sources is not possible, but an accurate extrapolation as function of frequency (and time) based on other independent measurements is certainly possible. These sources also provide the advantage of high brightness temperatures (a few 1000 K instead of 100-200 K for planets and asteroids), making them more suitable as calibrators at high angular resolution.

3.5 Quasars

Many quasar catalogs exist at radio wavelengths: VLA, PARKES, JVAS, IRAM with a total of more than 10000 sources. Using principally in the JVAS catalog, quasar flux distribution have been measured accurately at 86 GHz with the IRAM PdBI by [Neri et al. 1998], in two 20×20 degrees square fields. The average flux obtained for quasar to source distance equal to 2, 4 and 7 degrees are 0.1, 0.5 and 1.5 Jy respectively. The theoretical spectral index is in the range of -0.5;-1.0 which corresponds to synchrotron radiation. However, for our cm–flat spectrum selected spectra, the average spectral index is equal to -0.5.

The synchrotron emission process implies that continuum flux is polarized. Measurement at mm/submm wavelengths gives typical polarization in the range of 0-5%, although some quasars like 3C279 display higher polarization (up to 40 %). Quasars usually have a compact core. VLBI measurement indicate typical sizes of $\sim 0.001''$ [Bloom et al. 1999], but a fraction of the flux could come from the radio jet, with sizes of $0.01''$ or more. Self calibration of the quasar structure (or filtering of the baseline range) may be required on the longest ALMA baselines before these quasars can be used as amplitude (and phase) calibrators.

Strong quasars with known spectral index are needed for Bandpass calibration. Table 1 is a list of known strong quasars (with high flux at submm wavelengths) observable by ALMA. These quasars are of course variable, but on average the 4 strongest are: 3C273, 3C279, OV-236, and 3C454.3 Extrapolation of their fluxes at 850 GHz gives fluxes between 2 and 4 Jy. At the Chajnantor site, given the variety of hour angle and declination, one of them will be available at anytime for bandpass calibration.

Quasar variability happens on all time scale [Steppe et al. 1993], but the most significant variations have been measured on timescales of months to years. Maximum

Table 1: Strongest quasars at mm/submm wavelengths. These averaged fluxes were measured between 1985-1993 by [Steppe et al. 1993] and can vary by 50%. These values are in agreement with more recent (1998-2000) IRAM observations.

Source	α(J2000)	δ(J2000)	Flux@90	flux@230	SpI	flux@850
1226+023—3C273	12:29:06.69985	02:03:08.596	20.0	10.0	-0.7	3.8
1253-055—3C279	12:56:11.16644	-05:47:21.523	20.0	10.0	-0.7	3.8
1334-127—OP-158.3	13:37:39.78281	-12:57:24.692	6.0	3.0	-0.7	1.1
1641+399—3C345	16:42:58.81020	39:48:36.995	6.0	3.0	-0.7	1.1
1730-130—NRAO530	17:33:02.70580	-13:04:49.547	5.0	3.0	-0.5	1.5
1921-293—OV-236	19:24:51.05610	-29:14:30.120	9.0	5.0	-0.6	2.2
2145+067	21:48:05.45899	06:57:38.606	5.0	2.5	-0.7	1.0
2223-052—3C446	22:25:47.25951	-04:57:01.389	5.0	2.5	-0.7	1.0
2251+158—3C454.3	22:53:57.74830	16:08:53.563	7.0	5.0	-0.3	3.1

Table 2: Calibrator Flux (mJy) computed for several frequencies and calibration sources. $Q_{\rm band}$ is the strong quasar used as bandpass calibrator. Q_2, Q_4, Q_7 are quasars located at 2, 4 and 7 degrees from the source. *Star* is a supergiant star, *Ast* is an asteroid, *Sat* is a giant planet (Jupiter or Saturn) large satellite.

ν	$Q_{\rm band}$	Q_2	Q_4	Q_7	*Star*	*Ast*	*Sat*
(GHz)	Flux Density (mJy)						
43.	7800	145	720	2200	.1	1.7	70
90.	6000	100	500	1500	.4	7.7	306
230.	4100	62	310	940	2.8	50.0	2000
350.	3500	51	250	760	6.4	116.0	4630
410.	3300	47	235	700	8.8	159.0	6360
690.	2700	36	180	540	25.0	450.0	18000
850.	2400	32	160	490	37.9	680.0	27300

variations occurs through bursts, where an increase of 50% of the intensity in a month has been observed (i.e 1.7% per day). More typical intensity variations of 50% are observed with timescales of a year (i.e 0.15% per day). Blazars are the most variable (intraday variation of 5% at $\lambda = 2$ cm [Qian et al. 1991]) and should be avoided; they also tend to display high polarization (e.g. 3C279 unfortunately).

3.6 Conclusions

Planets, asteroids, stars and quasars can be used calibrators for ALMA. The choice of one observable calibration source at a given frequency is a compromise between their flux and size and the ALMA sensitivity and spatial resolution. The typical flux values are given in Table 2

Planets are the only primary calibrator for mm/submm, but their flux densities

are not yet known with an absolute uncertainty better than about 5%. All the other mm/submm continuum sources can be used as secondary calibrators. High accuracy measurements of these secondary calibrators will be needed to measure properly their flux in the mm/submm range. Most of the relative weak calibration source, as stars, could be measured with enough accuracy probably only with ALMA. Before the use of these secondary calibrators, some spectra modeling will be needed to improve our knowledge of their flux variations as function of the frequency.

Since part of the relative amplitude calibration may be performed observing quasars, their polarization must be taken into account. The final absolute accuracy will depend of the measurements relative uncertainties (1% requested), and the absolute accuracy of primary calibrators. Long term consistency at the 2% level should be easy to obtain at mm wavelengths. The absolute flux scale, however, is currently undetermined at the 5% level.

Spectral index knowledge will be required in many cases for an appropriate calibration. In the worst case, DSB operations near 90 GHz, the most extreme frequencies sampled by the receiver will be separated by 24 GHz. In order to have a Γ % accuracy on the relative gain at these two frequencies, the spectral index of the reference calibrator should be known with an uncertainty of less than 0.04Γ. For $\Gamma = 1$, this precision on the spectral index could be obtained from two measurements at 100 and 350 GHz with 3 % accuracy, or between 100 and 650 GHz with 5 % accuracy. Conversely, a prediction at 650 GHz to $\Gamma = 1$ % from a 100 GHz flux measurement requires a spectral index accurate to 0.005.

For further use, we shall express the calibration source flux dependence in frequency in terms of a *spectral index* α as

$$S_\nu(\nu) = S_{100} \left(\frac{\nu}{100\mathrm{GHz}}\right)^\alpha \tag{1}$$

where S_{100} is the source flux at 100 GHz. Unless otherwise specified, for all numerical applications, observation frequencies will be given in units of 100 GHz, and bandwidths in units of 1 GHz.

4 Weather statistics

Weather statistics are needed to estimate properly the different weather conditions expected at the ALMA site. The weather statistics of the ALMA site presented in Table 3 are based on different measurements: meteo station, radiosonde, FTS and 12 GHz interferometer (see `http://www.tuc.nrao.edu/mma/sites/`). Extrapolation from this table indicates that about 10% of the time will have precipitable water vapor of less than 0.3 mm, suitable even for the highest frequency observations.

Table 3 does not represent the correlation between the various parameters. We have attempted to first order to do so in our adopted atmospheric parameters when computing the ALMA sensitivity as indicated in Table 5. A drawback of the current approach is that we do not consider phase stability in this analysis. This is not a critical issue for low

Table 3: Weather statistics at the ALMA site

	Time (%)		
	25	50	75
Opacity at 225 GHz	0.037	0.061	0.117
Precipitable Water Vapor (mm)	0.7	1.2	2.3
Pathlength Rms on 300-m baseline (μm)	123	254	531
Temperature (°C)	-7.6	-2.4	3.2
Local Wind Speed (m/s)	3.1	6.4	10.3

Table 4: Optimum frequency for observations versus weather conditions and percentage of observing time

Cumulative time(%)	pwv (mm)	Freq (GHz)	% total time
99	5.0	43–90	25
75	2.3	230	25
50	1.2	350	25
25	0.7	410	15
10	0.3	690–850	10

frequency observations (< 400 GHz), but could be a serious problem for submillimeter observations, since high transparency conditions are not necessarily related to good phase stability.

Table 5: Adopted percentiles for the computation of the system temperatures. Note that this differ from Table 3 by trying (grossly) to account for correlations between opacity and temperature.

Percentile	τ(225 GHz)	Water vapor		Temperature	Observing
		Max.	Typical		Frequency
75 %	0.117	< 2.3 mm	2.3 mm	+3°C	< 250 GHz
50 %	0.061	< 1.2 mm	1.2 mm	0°C	< 370 GHz
25 %	0.037	< 0.7 mm	0.5 mm	-5°C	700 GHz

5 Sensitivity

The single-baseline flux sensitivity is defined by the standard noise equation

$$\sigma_b = \frac{\mathcal{J}}{\eta_c \eta_p} \frac{T_{\rm sys}}{\sqrt{2\Delta\nu t}} \tag{2}$$

where $\mathcal{J}$ is the Jy/K conversion factor of the antenna, related to the collecting area A and aperture efficiency η_a by

$$\mathcal{J} = \frac{2k}{\eta_a A} \tag{3}$$

$T_{\rm sys}$ is the system temperature, η_c is the correlator efficiency, η_p is the efficiency resulting from short term phase noise (instrumental and atmospheric), $\Delta\nu$ the bandwidth and t the integration time. We shall use $\eta_c\eta_p = 0.85$ and

$$\eta_a = \eta_i \exp\left[-\left(4\pi\frac{\sigma}{\lambda}\right)^2\right] \tag{4}$$

where $\eta_i = 0.8$ is the illumination efficiency, and $\sigma = 20\mu$m the rms surface error.

[Lucas 1998] showed that the **amplitude gain** noise σ_g is related to the baseline sensitivity σ_b through the baseline signal to noise ratio on a point source of flux S_ν by

$$\sigma_g = 2\frac{\sigma_b(\Delta\nu, t)}{S_\nu}\sqrt{\frac{2N-3}{2(N-1)(N-2)}} \simeq 2\frac{\sigma_b}{S_\nu\sqrt{N}} \tag{5}$$

where N is the number of **antennas**, $\Delta\nu$ the bandwidth, t the integration time.

The **phase gain** σ_ϕ noise is simply

$$\sigma_\phi \text{ (radians)} = \sigma_g \quad \sigma_\phi\ (^\circ) \simeq 57.3\sigma_g \tag{6}$$

For further numerical applications, we define the quantity σ_0 as

$$\sigma_0 = 2\sigma_b(\Delta\nu = 1 \text{ GHz}, t = 1 \text{ s})\sqrt{\frac{2N-3}{2(N-1)(N-2)}} \tag{7}$$

hence

$$\sigma_g = \sigma_\phi = \frac{\sigma_0}{S_\nu}\frac{1}{\sqrt{\Delta\nu(\text{GHz})t(\text{s})}} \tag{8}$$

From now on, we shall express all bandwidths in GHz, all integration times in seconds, and all flux densities in Jy, unless specifically quoted.

To compute σ_0, let us first compute the typical system temperature. We assume the standard ALMA specification for receiver temperature:

$$T_{\rm rec}(\nu) = 6h\nu/k + 4 \text{ K} \quad (\nu < 400\text{GHz}) \quad \text{and} \quad T_{\rm rec}(\nu) = 10h\nu/k + 4 \text{ K} \quad (\nu > 400\text{GHz})$$

for single sideband receivers (rejection better than 10 dB), and

$$T_{\rm rec}(\nu) = 3h\nu/k \text{ K} \quad (\nu < 400\text{GHz}) \quad \text{and} \quad T_{\rm rec}(\nu) = 5h\nu/k \text{ K} \quad (\nu > 400\text{GHz})$$

for double sideband receivers.

We also assume the forward efficiency is falling down from 0.95 at low frequencies to 0.90 at 900 GHz (as ν^2). This assumption follows the observed behaviour of existing antennas, and should be verified by measurements on the prototype antennas.

The atmospheric conditions are taken from the weather statistics percentiles, with temperature adjusted to account (to first order) for the imperfect correlation between temperature and opacity. We assume dynamic scheduling will match the observed frequency to the appropriate observing conditions, more precisely that observations above 370 GHz will be done only in the 25 % best observing time, observations between 270 and 370 GHz only in the 50 % best observing time, and "low" frequency observations in the remaining available good weather (see Table 5). The frequency setup is done in such a way to minimze the image sideband contribution to noise whenever possible. Note that under these conditions, the SSB receivers still provide better performances than the DSB receivers (for spectral line observations, but not always for continuum work), even at submm wavelengths.

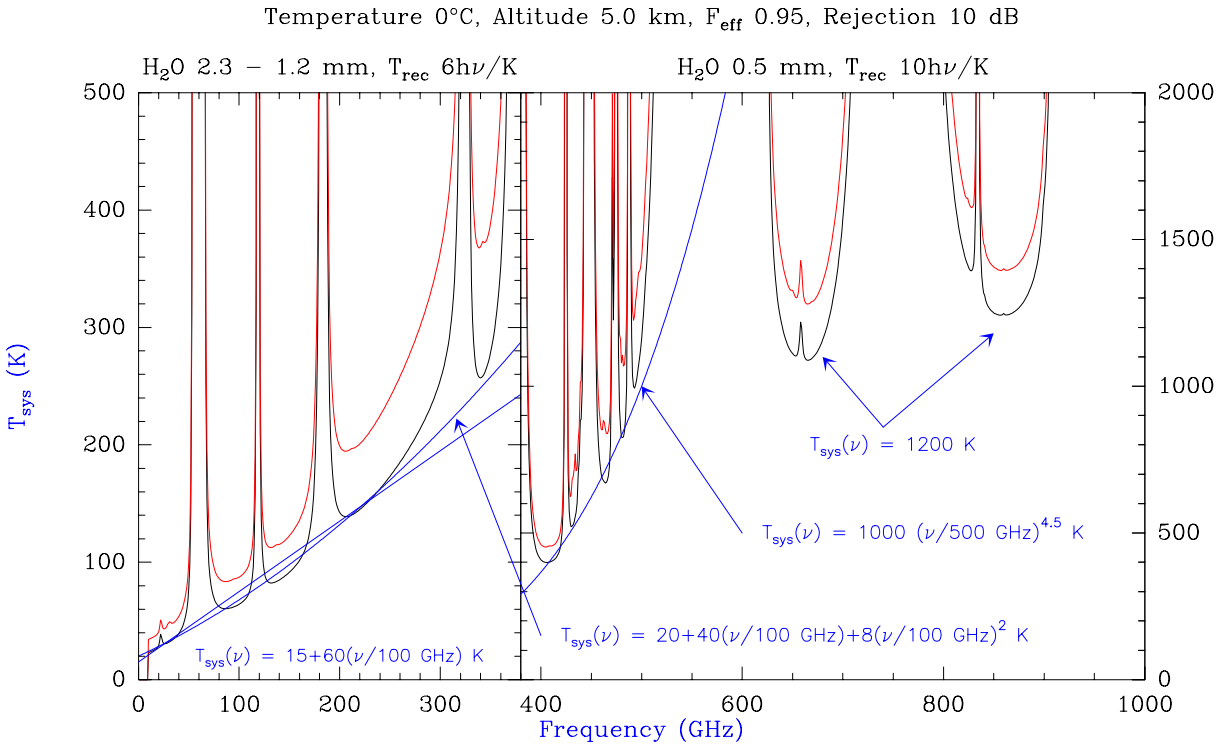

Figure 1: Expected typical system temperatures with ALMA. The black curves correspond to Single Side Band tuned receivers (image rejection 10 dB), while the red curves correspond to Double Side Band tuned receivers. Several approximation curves are indicated. Created by `default_tsys.astro`

Figure 1 gives the corresponding expected system temperature. Several "simple" approximations can be given for $T_{\rm sys}$ as function of frequency provided the observing

Table 6: ALMA array sensitivity as function of frequency and precipitable water vapor (pwv), for 1 second integration time and 8 GHz bandwidth. $\mathcal{J}$ is the antenna gain as given from Eq.3. σ_b and σ_p are the total array and baseline sensitivity, respectively, for point sources. σ_0 is the single antenna sensitivity given for 1 GHz bandwidth.

Frequency (GHz)	pwv (mm)	T_{sys} (K)	$\mathcal{J}$ Jy/K	σ_b (mJy)	σ_0 (mJy)	σ_p (mJy)
43.	2.3	45	30.5	12.8	9.1	0.28
90.	2.3	70	30.5	19.9	14.2	0.44
230.	2.3	150	31	43.2	30.9	0.96
350.	1.2	250	33	76.7	54.9	1.71
410.	0.5	400	35	130.2	93.2	2.90
690.	0.5	1200	40	446.4	319.5	9.94
850.	0.5	1200	50	558.0	399.3	12.43

frequency is far enough from an atmospheric line (of O_2 or H_2O).

$$T_{\rm sys}(\nu) = 15 + 60(\nu/100\ {\rm GHz})\ \ {\rm K} \quad ({\rm for}\ \ \nu < 370\ {\rm GHz}) \tag{9}$$

$$T_{\rm sys}(\nu) = 1000(\nu/500\ {\rm GHz})^{4.5}\ \ {\rm K} \quad ({\rm for}\ \ 370 < \nu < 500\ {\rm GHz}) \tag{10}$$

$$T_{\rm sys}(\nu) = 1200\ \ {\rm K} \quad ({\rm for}\ \ \nu > 600\ {\rm GHz}) \tag{11}$$

We use an aperture efficiency η_a derived from the 20 μm surface accuracy specification, the 12-m diameter, and assuming a 2.5 % blockage. The single baseline point source sensitivity as function of of frequency is given in Figure 2. It is normalized to 1 second of integration and 1 GHz of bandwidth, to provide convenient scaling for further use. The value of σ_0 for $\nu \sim 90 - 100$ GHz is about 14 mJy. Values of σ_0 at the band centers at given in Table 6, together with the baseline noise σ_b and array point source sensitivity σ_p for 8 GHz bandwidth

6 Atmospheric Transparency and Receiver Gain

The atmospheric amplitude calibration was studied by [Yun et al. 1998], [Bock et al. 1998], [Mangum 2000], [Plambeck 2000]. In ALMA memo 371, [Guilloteau & Moreno 2001] we explicited some of the specifications of the two most promising techniques. We found that the semi-transparent vane calibration method provides a number of technical advantages (simplicity, location, and possibility to calibrate it). We discuss here the calibration uncertainties related to atmospheric modeling in the two methods.

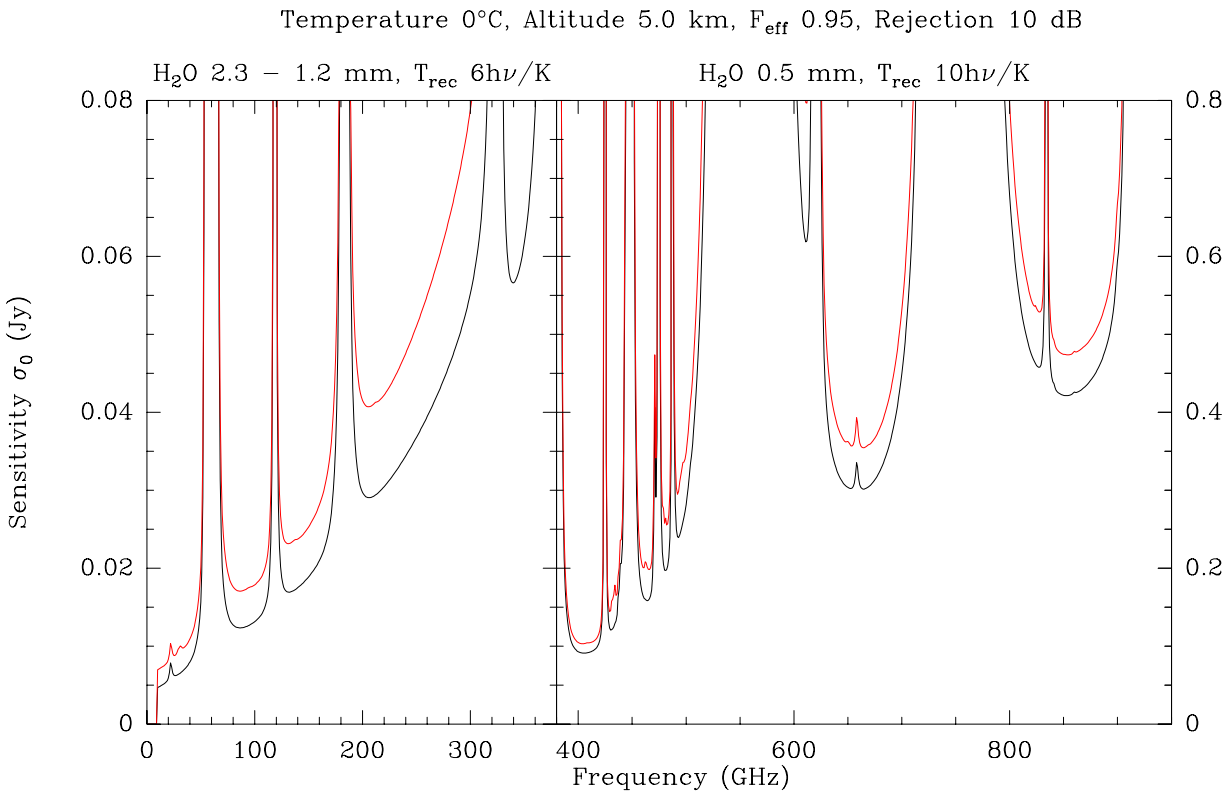

Figure 2: Single antenna sensitivity (σ_0) as defined in Eq.7 for 1 second integration and 1 GHz of bandwidth for 64 12-m antennas. Created by `default_sens.astro`

6.1 Semi-Transparent vane calibration

In the semi-transparent vane calibration method, the measurement equations are (see ALMA memo 371 [Guilloteau & Moreno 2001] for the notations):

$$\begin{aligned} P_{\rm sky} &= K(T)(T_{\rm rec} + J_{\rm sky}) \\ P_{\rm load} &= K(T)(T_{\rm rec} + fJ_{\rm load} + (1-f)J_{\rm sky}) \\ C_{\rm source} &= K(T)\eta e^{-\tau} T_A \end{aligned} \tag{12}$$

This is a one-load calibration method, for which the source antenna temperature is given by

$$T_A = fT_{\rm cal}\frac{C_{\rm source}}{P_{\rm load} - P_{\rm sky}} \tag{13}$$

where $T_{\rm cal}$ is the calibration temperature [Ulich & Haas, 1976]

$$\begin{aligned} T_{\rm cal} &= J^s_{\rm spill} - J^s_{\rm bg} + g(J^i_{\rm spill} - J^i_{\rm bg}) \\ &+ (e^{\tau_s} - 1)(J^s_{\rm spill} - J^s_{\rm m} + g(J^i_{\rm spill} - J^i_{\rm m})) \\ &+ g(e^{\tau_s - \tau_i} - 1)(J^i_{\rm m} - J^i_{\rm bg}) \\ &+ \frac{e^{\tau_s}}{\eta}(J^s_{\rm load} - J^s_{\rm spill} + g(J^i_{\rm load} - J^i_{\rm spill})) \end{aligned} \tag{14}$$

where $J_{\rm x}^j$ is the Rayleigh-Jeans equivalent temperature of a black body at temperature $T_{\rm x}$ and frequency ν_j. j takes values s or i for signal or image bands respectively.

$$J_{\rm x}^j = \frac{h\nu_j}{k}\frac{1}{e^{h\nu_j/kT_{\rm x}}-1} \tag{15}$$

$J_{\rm m}$ is the effective temperature of the atmosphere (the physical temperature of the absorbing layers, not the apparent brightness temperature). Calibration requires the knowledge of calibration device related parameters (f and $J_{\rm load}$), antenna related parameters (η and $J_{\rm spill}$), receiver related parameters (g) and atmospheric parameters ($J_{\rm m}$ and τ_s and τ_i). Having so many parameters looks a priori complex and error prone, but we shall see that $T_{\rm cal}$ actually depends only marginally on some of them.

6.1.1 Absolute errors

The expression of $T_{\rm cal}$ has two useful limiting cases, which can be very helpful in deriving the major uncertainties: the homogeneous temperature case $J_{\rm load} \simeq J_{\rm m} \simeq J_{\rm spill}$ for which

$$T_{\rm cal} \simeq (1+g)J_{\rm m} \tag{16}$$

and the low opacity case $\tau \ll 1$, for which

$$T_{\rm cal} \simeq \frac{1+g}{\eta}(J_{\rm load} - (1-\eta)J_{\rm spill}) = (1+g)J_{\rm spill} + \frac{1+g}{\eta}(J_{\rm load} - J_{\rm spill}) \tag{17}$$

$T_{\rm cal}$ is thus of order 300 K, for a single sideband system ($g = 0$). At low frequencies, where τ is small, the error on $T_{\rm cal}$ can be simply derived from the partial derivatives of Eq.17

$$\begin{aligned}
\frac{\partial T_{\rm cal}}{\partial g} &= J_{\rm spill} + (J_{\rm load} - J_{\rm spill})/\eta \\
\frac{\partial T_{\rm cal}}{\partial \eta} &= (1+g)(J_{\rm load} - J_{\rm spill})/\eta^2 \\
\frac{\partial T_{\rm cal}}{\partial J_{\rm spill}} &= (1+g)(\eta-1)/\eta \\
\frac{\partial T_{\rm cal}}{\partial J_{\rm load}} &= (1+g)/\eta
\end{aligned}$$

Orders of magnitude of the errors are easy to obtain with this expression. The load temperature should be measurable with 0.2 K accuracy, giving $\delta T_{\rm cal}({\rm load}) \simeq 0.2$ K, g with 0.5 % precision $\delta T_{\rm cal}(g) \simeq 1.5$ K, and $\eta \simeq 0.95$ to about 0.2% precision, $\delta T_{\rm cal}(\eta) \leq 0.05$ K. The error on $J_{\rm spill}$ is less straightforward, since part of the spillover is in the receiver cabin, while part is towards the antenna or the ground, at the ambient temperature, but even assuming an error of up to 6 K on this value, the contribution to the error on $T_{\rm cal}$ is small because of the factor $\eta - 1$, $\delta T_{\rm cal}({\rm spill}) \leq 0.3$ K. Sideband gain ratio taken apart, the expected precision error is thus $\delta T_{\rm cal} \lesssim 0.4$ K, i.e. better than 0.2 %

Similarly, for high opacities where the other approximation is reasonably valid, one immediately sees than the dominant error is on the evaluation of $J_{\rm m}$, and of course g. [Plambeck 2000] estimates an error of order 5 K (i.e. 2%) on $J_{\rm m}$ (see also [Pardo et al. 2001]).

6.1.2 Elevation dependence

Another important aspect is the derivative of $T_{\rm cal}$ relative to the opacity τ. It will play a role in 1) the variation of the calibration from one antenna to the other, 2) the variation of the calibration as function of time due to varying opacity, and 3) elevation dependent errors which could play a role when bootstrapping a flux measurement from observations at different elevations. For simplicity, let us neglect the opacity difference between the image and signal band, $\tau \approx \tau_s \approx \tau_i$

$$\begin{aligned} \frac{\partial T_{\rm cal}}{\partial \tau} &= e^{\tau}(1+g)(J_{\rm spill}-J_{\rm m}) + \frac{e^{\tau}}{\eta}(1+g)(J_{\rm load}-J_{\rm spill}) \\ &\quad -(e^{\tau}-1)(1+g)\frac{\partial J_{\rm m}}{\partial \tau} \end{aligned} \tag{18}$$

$$\frac{\partial T_{\rm cal}}{\partial \tau} \approx \frac{e^{\tau}}{\eta}(1+g)\left[(1-\eta)J_{\rm spill} + (J_{\rm load}-\eta J_{\rm m})\right] \tag{19}$$

where we have neglected the implicit (but small) dependence of the effective temperature of the atmosphere $J_{\rm m}$ on the opacity in the last equation. We typically have $J_{\rm spill} = 270$ K, $J_{\rm load} = 290$ K and $J_{\rm m} = 260$ K giving an opacity derivative of about 70 K per neper, times the $(1+g)e^{\tau}/\eta$ factor.

At low frequency, the derivative is about 70 – 80 K, while for high frequency observations where the opacity could be of order 1, this goes up to about 160 K. Since $T_{\rm cal}$ is of order 300 K, it can be seen that the maximum opacity change is about $0.04\,\Gamma$ at mm wavelengths for a relative precision $\Gamma\,\%$. At submm wavelengths, the maximum tolerable opacity change is only $0.015\,\Gamma$.

We can apply these values to derive

1. The antenna to antenna variation: using the median pathlength fluctuations, 250 μm on a 300 m baseline, [Plambeck 2000] estimate a maximum variation $\delta\tau/\tau \approx 0.03$ for 1.5 km, which is below the tolerance level at mm wavelengths, but a factor 2 above at submm wavelengths.

2. The time variation: it can be related through the Taylor hypothesis to pathlength fluctuations using the mean wind speed. Again, a value of $\delta\tau/\tau \approx 0.03$ is found for a timescale of about 3 minutes. Calibration should then be performed more frequently. Note that a differential opacity correction based e.g. on the WVR measurement is easy to implement.

3. The elevation tolerance in case of inaccurate opacity correction. This is relevant in all relative amplitude calibration schemes, including flux bootstrapping from a primary calibrator. The tolerable change in airmass can be derived from the uncertainty on the opacity and the required precision level from

$$\delta{\rm Airmass}\ \delta\tau_z \left(\frac{1}{T_{\rm cal}}\frac{\partial T_{\rm cal}}{\partial \tau}\right) < \Gamma \tag{20}$$

   where τ_z is here the zenith opacity. At mm wavelengths, where $1/T_{\rm cal}\partial T_{\rm cal}/\partial\tau$ is quite small (of order 0.25), the elevation can change quite significantly before

the error on the opacity becomes a significant effect. At submm wavelengths, $1/T_{\rm cal}\partial T_{\rm cal}/\partial\tau \approx 0.5$. For $\delta\tau_z \lesssim 0.1$, the airmass tolerance is about 0.2, corresponding to about 8° near 45° elevation. Accurate relative amplitude calibration will be possible within this elevation range.

Given these numbers, applying a single value of $J_{\rm m}$ and τ derived from either the mean of all antennas, or an independent atmospheric sounding device, will give best results at mm wavelengths. An independent sounding device would have the advantage of not using precious observing time, as well as most likely providing more accurate measurements.

6.2 Dual-Load Calibration Method

With two loads located in the subreflector, the calibration equations are

$$P_{\rm hot} = K(T)(T_{\rm rec} + fJ_{\rm hot} + J_{\rm sky} + g_s\eta e^{-\tau}T_A) \quad (21)$$

$$P_{\rm amb} = K(T)(T_{\rm rec} + fJ_{\rm amb} + J_{\rm sky} + g_s\eta e^{-\tau}T_A) \quad (22)$$

$$C_{\rm source} = K(T)g_s\eta e^{-\tau}T_A \quad (23)$$

g_s is here the signal gain, normalized such that $g_s + g_i = 1$, i.e. $g_s = 1/(1+g)$ when expressed in terms of sideband gain ratio. The calibration temperature is

$$T_{\rm cal} = (1+g)\frac{e^{\tau}}{\eta}f(J_{\rm hot} - J_{\rm amb}) \quad (24)$$

Calibration thus requires the knowledge of 6 independent parameters: the two load temperatures $J_{\rm hot}$ and $J_{\rm amb}$, the beam coverage fraction f (discussed in Memo 371 [Guilloteau & Moreno 2001]), and the forward efficiency η, the sideband gain ratio g and the atmospheric transmission τ.

6.2.1 Absolute Errors

We can easily compute the partial derivatives of Eq.24 to get the typical errors in the calibration due to τ, η and g

$$\frac{\partial T_{\rm cal}}{\partial\tau} = T_{\rm cal}\ ; \qquad \frac{\partial T_{\rm cal}}{\partial\eta} = -\frac{T_{\rm cal}}{\eta}\ ; \qquad \frac{\partial T_{\rm cal}}{\partial g} = \frac{T_{\rm cal}}{1+g} \quad (25)$$

Compared to the semi-transparent vane calibration, the error introduced by the uncertainty on g is identical, while the errors introduced by the uncertainty on η and τ are larger (by a factor 2 to 10). Accordingly, the absolute calibration with the dual-load method is intrinsically less accurate than the vane calibration technique.

6.2.2 Elevation Dependence

From Eqs.20 and 25, the tolerance on the change in airmass before the opacity correction becomes too uncertain is simply given by

$$\delta{\rm Airmass} = \Gamma/\delta\tau_z \quad (26)$$

Again, at mm wavelengths, this is not a serious issue, but at submm wavelengths, a precision of $\Gamma = 1\,\%$ restricts the airmass change to 0.1 (or about 4° near 45° elevation) for a typical error on the opacity of 0.1. If, as argued by [Plambeck 2000] and [Pardo et al. 2001], the typical opacity error is better than 0.05, an elevation tolerance of about 7° would still be acceptable.

7 Bandpass, Sideband gain ratio, and Delays

In previous section, we have seen that the sideband gain ratio of the receiver plays a major role in the accuracy of the calibration. This gain ratio is only one aspect of the more general **Bandpass Calibration**. Bandpass calibration can be decomposed in several steps

1. Delay measurement (i.e. average phase slope over the receiver band)
2. Sideband gain ratio measurement
3. Fine scale bandpass structure due to backend (at the observed spectral resolution, which we call the **User configuration**)
4. Large scale bandpass structure due to frontend and antenna

We shall evaluate the time required for these various steps.

7.1 Delay measurement

This has to be performed both at the observing frequency $\nu_{\rm obs}$ and at the calibration frequency $\nu_{\rm cal}$. A strong point source is sufficient for this. It can be located far away from the observing direction. The delay error is

$$\delta\tau_g = \frac{2}{\pi\Delta\nu_{\rm B}}\sigma_\phi \tag{27}$$

where $\Delta\nu_{\rm B}$ is the available bandwidth for the delay measurement, i.e. 8 GHz in our case (the two polarizations have to be calibrated independently). Inserting numerical values, we obtain

$$\delta\tau_g\ ({\rm nsec}) = 0.080\frac{\sigma_0}{S_\nu}(\Delta\nu_{\rm B}\ ({\rm GHz}))^{-1.5}t^{-0.5} \tag{28}$$

Using $S_\nu = 1$ Jy as a typical number, and $\Delta\nu = 8$ GHz (since each polarization must be calibrated separately), we obtain $\delta\tau < 10^{-4}$ nsec at all mm frequencies in just 1 second of integration time, and $\delta\tau < 2\,10^{-3}$ nsec at submm frequencies. The latter value guarantees less than 6 degree phase slope across the full bandwidth (8 GHz).

7.2 Sideband gain ratio

This may vary on scales of a few 100 MHz, e.g. $\Delta\nu_{\rm G} = 250$ MHz or so. The error on sideband gain ratio is

$$\frac{\delta T_{\rm cal}}{T_{\rm cal}} = \frac{\delta g}{1+g} = \sigma_g = \frac{\sigma_0}{S_\nu\sqrt{\Delta\nu_{\rm G}t}} \tag{29}$$

where g is the image to signal gain ratio. The required time is

$$t_{\rm gain} = \left(\frac{100\sigma_0}{\Gamma S_\nu}\right)^2 \frac{1}{\Delta\nu_{\rm G}} \tag{30}$$

where Γ is the required calibration accuracy (in percent). Using $S_\nu = 1.5$ Jy as a typical number (Q_7 quasar), and $\Delta\nu = 0.25$ GHz, gives a precision of $\Gamma = 1\,\%$ in 4 seconds of time at 100 GHz. At submm wavelengths, where σ_0 is 30 times larger and the flux weaker, this becomes more than 1000 times longer.... Using the strongest quasars ($Q_{\rm band}$) allows to bring back the time to about 7 minutes. Note that the required calibration time goes as $1/\Gamma^2$.

The spectral index of the calibration source must be taken into account in the derivation of the sideband gain ratio by such a method. In the worst case conditions (near 93 GHz) the difference in frequency between the two sidebands reaches 30 %. The spectral index should thus be known to better than 0.04Γ at this frequency; the tolerance decreases linearly with observing frequency. It should also be noted that when the signal and image band opacities differ, there is a coupling between the measurement of the sideband gain ratio and the atmospheric calibration. An iterative process could be needed to solve the problem (although a single measurement is sufficient).

7.3 Fine scale bandpass

Standing waves excepted, the fine scale bandpass structure can be referenced to large scale bandpass structure by observing at any frequency, since it is backend dependent only. To calibrate it, one could observe a strong, low frequency, source with the **User configuration** and with the correlator in broad band mode. This does not require any special device, and makes no assumption about the backend properties. A differential delay may appear during this calibration step, see Section 7.1 for its calibration. The typical error will be $\sigma\phi = \sigma_g = \sigma_0/(S_\nu\sqrt{\Delta\nu_{\rm F} t})$. Using the stronger calibrators, $S_\nu = 6$ Jy, an integration time of one minute is required for 1% precision for a resolution of 1 MHz. The integration time goes as $1/\Gamma^2$.

Another potential method is the use of a frequency scanning, coherent emission device located in the antenna subreflector. A few picoWatt of coherent signal would already give a million times stronger signal than the "strong" calibrator mentioned above. However, it would be required to control the dependence of this power level as function of frequency to better than 1 % accuracy, which may prove difficult because of standing waves. Note that the standing waves which may affect this calibration signal are neither the ones affecting the source signal, nor the ones affecting the sky and antenna background.

Eventually, we may rely on the properties of digital filtering to perform the fine scale bandpass calibration. If all filters are digital, there should be no phase distortion and a predictable amplitude response pattern for the narrow filters. With a stable backend, this fine scale bandpass structure is reproducible and can be tabulated. The only difficulty is the large number of correlator configurations ...

7.4 Large scale bandpass

The large scale bandpass structure is tuning dependent, and hence has to be calibrated *at the observing frequency*. With receivers having an instantaneous bandwidth of 4 to 8 GHz, and samplers at 4 GHz clock rate, we do not expect structures on scales smaller than about 300 MHz. Our goal is thus to obtain Γ % accuracy on such bandwidths. The calibration scheme must be able to provide enough sensitivity to reach this accuracy. The integration time goes as $1/\Gamma^2$.

The numbers to be considered here are similar to those for the sideband gain ratio measurement. Astronomical sources are quite suitable to give this precision at mm wavelengths, but far too faint at submm wavelengths. This leaves two possibilities only: using the reference signal in the subreflector, or relaxing the requirement on Γ.

The large scale bandpass calibration can use the same data than the sideband gain ratio measurement. However, linking it to the fine scale bandpass data also requires a bandpass / sideband ratio measurement at the calibration frequency ν_{cal}.

7.5 Standing waves

In the above discussion, we have ignored the possible standing waves which may distort the bandpass shape. With the ALMA antenna parameters, frequency ripples due to standing waves will have a period of about 31 MHz. Sampling the standing wave pattern thus require a spectral resolution of order 2-3 MHz. Calibrating the pattern will be about 100 times longer than required for the large scale bandpass or sideband gain ratio. It will still be possible on astronomical sources (see Section 7.3) at mm wavelengths, but not at sub-mm wavelengths (however, this may not be required, see below).

There are several types of standing waves, which affect the signal differently.

1. The first type is a modulation of the antenna background. It affects the value of the system temperature, and thus the conversion from correlation coefficient measured by the correlator to correlated intensity as required for astronomical purpose.
2. A second type is a modulation of the transmission function of the source signal, which directly affects the correlated intensity.

The standing wave pattern may vary with elevation because of the elevation dependent deformations of the antennas. It could thus play some role in the relative amplitude calibration. Moreover, the patterns are independent between antennas. Hence, there will be an averaging effect, which will reduce the net effect on correlated intensities. This may bring the effect below the tolerable level. To remove the remaining baseline-based effect, it would be preferable to use an half-wavelength modulation scheme to reduce any standing wave pattern below the required precision level than to try to calibrate it.

Note that the amplitude of standing waves is inversely proportional to frequency. Accordingly, standing waves will mostly impact mm wavelengths observations. Detailed computations of the expected standing wave patterns based on the current antenna design are required to assess which strategy is best in handling this problem.

8 Pointing

For pointing calibration, we want the best rms on pointing errors. Pointing errors are related to the amplitude gain noise by

$$\sigma_\theta \propto \theta\sigma_g \tag{31}$$

where θ is the full width at half power primary beam width. The proportionality coefficient varies with the pointing measurement technique used (cross scans, three points, five points, circles, etc...) and can be optimized.

To compute the effective sensitivity, we shall use a semi-optimized five point method. In a five point method, with offset θ/a, we have

$$\sigma_\theta = \theta\sigma_g \frac{\sqrt{e}}{4\sqrt{\log 2}} f(a) \tag{32}$$

where $f(a)$ is a function of minimum value 1, reached for $a = \sqrt{8\log 2}$. With an appropriate cycle so that one out of 5 antennas is always pointed, the gain of each mispointed antenna is

$$B(a) = \exp\left[-\left(\frac{a2\sqrt{\log 2}}{\theta}\right)^2\right] \tag{33}$$

times the gain of each pointed antenna. Adding their contributions quadratically yields an improvement in sensitivity compared to the simple case of

$$\sqrt{((1/B(a))^2 + 4)/5}$$

With the value of a as above, $B = 1/\sqrt{e}$, this gain is $\sqrt{(4+e)/5}$

$$\sigma_\theta = \theta\sigma_g \frac{\sqrt{e}}{4\sqrt{\log 2}} \sqrt{\frac{5}{4+e}} \simeq 0.43\sigma_g\theta \tag{34}$$

Since the primary beam width is $\propto \nu^{-1}$, with a value of $\sim 62''$ at 100 GHz, the pointing error is

$$\sigma_\theta = 26'' \frac{\sigma_0}{S_{100}} \nu^{-\alpha-1} \tag{35}$$

In general, we will have to use quasars as pointing calibrators; in some circumstances, asteroids or major satellites could be used. The typical spectral index of a quasar is -0.3 to -0.7. Figure 3 gives the optimal pointing frequencies as function of spectral index and observation conditions (percentiles). This figure shows that the optimal frequency for pointing is near 100 GHz, whatever the observing circumstances. It also shows that there is little difference between the 3 mm window and 2 mm windows for this, so that it is not absolutely necessary to switch to the 3 mm receiver to calibrate 2 mm observations. The subscan time is given by

$$t = \left(\frac{26''}{\sigma_\theta}\frac{\sigma_0}{S_{100}}\right)^2 \frac{1}{\Delta\nu} \tag{36}$$

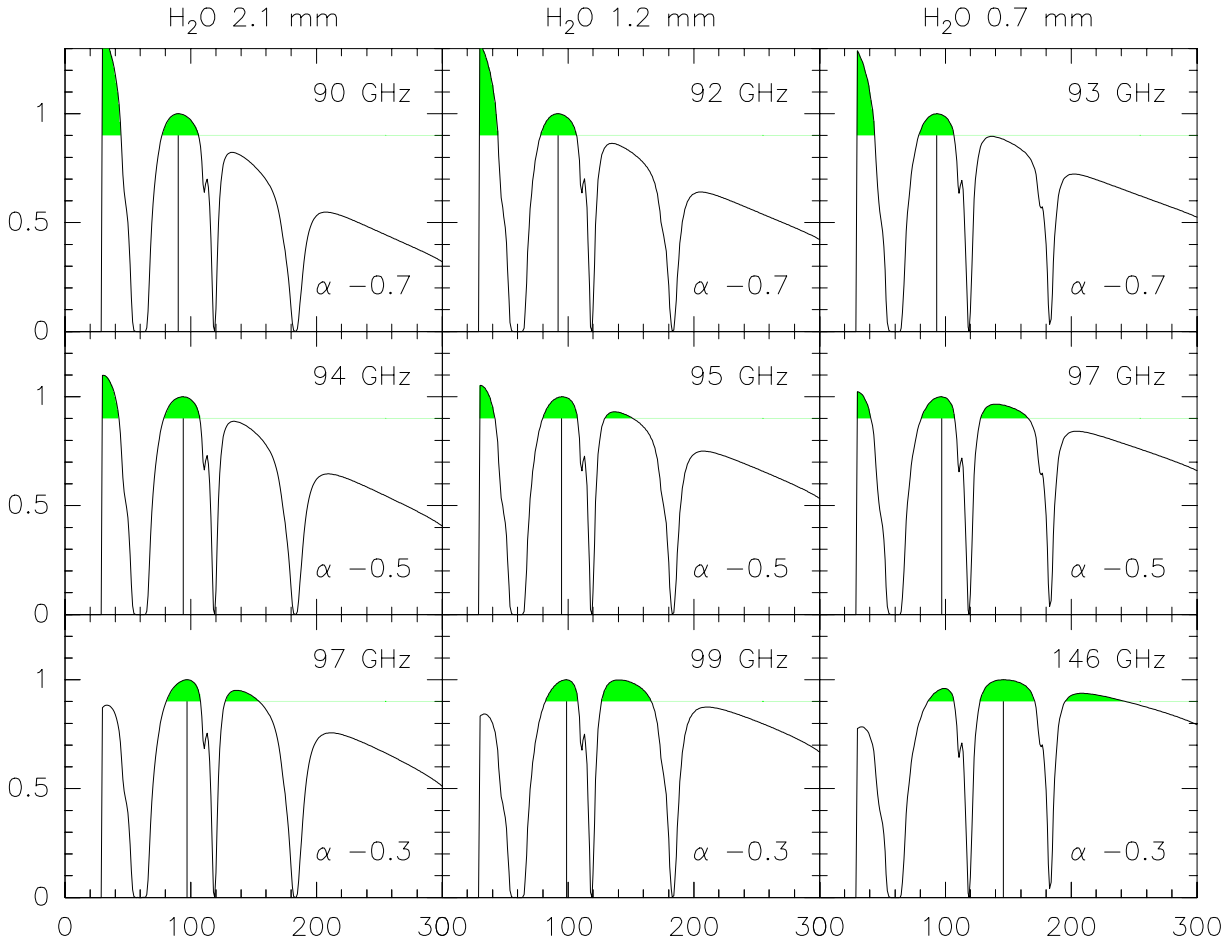

Figure 3: Relative sensitivity for pointing calibration as function of calibration $\nu_{\rm cal}$. Left column corresponds to low frequency observations, middle to 350 GHz observations, and right to submm observations. 3 different spectral index values have been used to derived the plots ($\alpha = -0.7, -0.5, -0.3$ from top to bottom). Created by `all_point.astro`

and for $\sigma_\theta = 0.25''$ pointing error in each direction (consistent with the goal of $0.7''$ global pointing error), it is 12 seconds on a 0.1 Jy source at 90 GHz with 16 GHz bandwidth. We should add dead times (1.5 s) between each subscan, plus time to move to the pointing calibrator (at 3°/s angular speed). The typical total time to point on a 0.1 Jy source is thus 70 seconds.

An alternative, much more attractive solution, is to derive a **local pointing model** by measuring several nearby sources. The antenna specification calls for a pointing accuracy of $0.6''$on a timescale of 30 minutes. In 30 minutes, due to earth rotation, the source position will drift 7 degrees on the sky. Hence, a local measurement 2 degrees away is not the most appropriate sampling of the pointing parameters. It is better to use a few (3–5) sources located between 4 and 7 degrees from the source. Since the typical flux of quasar at 4 degrees is about 0.5 Jy at 90 GHz, the required integration time per subscan goes down to 0.5 s. The observing time is thus totally dominated by antenna slew times. In a minute, it would be possible to observe 4 to 5 quasars, derive a local pointing model, and measure the effective pointing scatter (actual rms pointing

error). Since more than one direction is used, the pointing model could have a (local) dependence on Azimuth and Elevation, which could be applied for the source position until the next pointing measurement.

We used here an optimized 5 points method to estimate the integration time. A method scanning the antennas in a circle at the half-power of the primary beam would require similar integration times, but have less overhead.

9 Focus

For focus calibration, we want the best rms on pathlength errors. In an interferometer, a focus measurement is typically made by moving the subreflector to 3 or 5 different positions, proportional to some focus `Offset`. As for the pointing, interleaving the offsets between the various antennas maximizes the precision. Pathlength errors are related to the amplitude gain noise by

$$\sigma_{\rm focus} \propto \texttt{Offset}\ \sigma_g \tag{37}$$

The proportionality coefficient varies with the choice of the subreflector offsets and can be minimized. The minimization gives an `Offset` which is proportional to the observing wavelength.

For example, for a 3 point measurement, we can derive the optimal focus offsets from the Gaussian beam approximation. The waist of the beam is

$$w_0 = \frac{\lambda}{\pi} 2F\sqrt{0.115{\rm Te}} \tag{38}$$

where F is the secondary F ratio (8 for the ALMA antennas) and Te the edge taper in dB (10 to 12 for ALMA receivers). The focus curve is given by

$$k(Z) = \frac{1}{1+(\frac{Z\lambda}{2\pi w_0^2})^2} = 1/(1+x^2) \tag{39}$$

where Z is the **feed horn** displacement. For sub-reflector displacement z, we have to enter the magnification factor m^2+1. Hence $x = (z/z_0)$ with

$$z_0 = \frac{\lambda 8F^2 0.115{\rm Te}}{\pi(m^2+1)} = 1.4\ {\rm mm}\left(\frac{\lambda}{3\ {\rm mm}}\right) \tag{40}$$

The derivative of the focus curve is maximum for $x_{\rm opt} = 1/\sqrt{3}$, for which

$$z_{\rm opt} = 0.8\ {\rm mm}(\lambda/3\,{\rm mm}) \quad \text{and} \quad k(z_{\rm opt}) = 0.75 \quad \text{and} \quad k'(z_{\rm opt}) = \sqrt{27}/(8z_0) \tag{41}$$

and the focus error is related to the relative precision error by

$$\sigma_{\rm focus} = \sigma_g \frac{1}{\sqrt{2}k'(z_{\rm opt})} = z_0 4\frac{\sqrt{2}}{\sqrt{27}}\sigma_g = K\frac{\sigma_0}{S_{100}}\nu^{-\alpha-1} \tag{42}$$

giving $K = 1.5$ mm. Hence, focus measurement have the same dependence with frequency as pointing measurements. Thus, Figure 3 can also be used to derive the optimal

focus frequencies as function of spectral index and observation conditions (percentiles). Frequencies around 90-100 GHz are optimal.

The typical timescale can be computed from $\sigma_0(100\ \mathrm{GHz}) = 14$ mJy. A $\Gamma\,\%$ gain error due to focus corresponds to $\delta x = 0.1\sqrt{\Gamma}$, i.e.

$$\sigma_{\mathrm{focus}} = 0.14\ \ \mathrm{mm}\left(\frac{\lambda_{\mathrm{obs}}}{3\ \mathrm{mm}}\right)\sqrt{\Gamma}$$

Reaching $\Gamma = 1\,\%$ at the 3σ level for 900 GHz observations require an accuracy of about 5μm, corresponding to a signal to noise ratio of about 300:1. With a bandwidth of 16 GHz, and a source of 1 Jy (which can be found within 10 degrees of any source), this can be obtained in just 1 second of time per point.

However, there may be a somewhat better tradeoff for focus measurements when we take into account the time required to move the subreflector to the appropriate offsets. Since that time is proportional to the wavelength, slightly higher frequencies will be favored. Moreover, one may legitimately worry about measuring a difference of 5μm from a 0.8 mm physical displacement. Going to higher frequencies (e.g. 230 GHz) would also be preferable from this standpoint, at least when observing at submm wavelengths. The integration time per subscan would only slightly increase. In summary,

$$T_{\mathrm{focus}}(\mathrm{sec}) \simeq 3\left(\frac{\nu_{\mathrm{obs}}}{900\,\mathrm{GHz}}\right)^2\frac{1}{\Gamma} + \mathrm{motion\_time} + \mathrm{slew\_time} \tag{43}$$

is a reasonable estimate. Note that with a focus change rate of order 50 μm per hour, the focus may need to be checked every 7 minutes for high frequency observations. For 300 GHz observations, a check every 20 minutes is sufficient. Prediction of the focus change rate (which should be relatively easy, either from thermal monitoring of the antennas, or from empirical relations such as using the last measured rate averaged over all antennas) could help relaxing these numbers.

A last point which should be mentioned is the determination of the relative focus at the observing and calibration frequency. This requires measuring the focus at the observing frequency, rather than at the calibration frequency. In the worst case condition (900 GHz observations), where σ_0 is about 30 times larger than at 100 GHz, one would need several minutes if the focus was measured on a quasar. This would be problematic, because decorrelation losses due to atmospheric phase noise would not be negligible on such a time scale, and would bias the result. It will be much more efficient to measure that on planets in total power, using a fast scanning technique. Another alternative would be to use a Jupiter or Saturn satellite, which still benefits from the interferometric mode in the more compact configurations. Asteroids also are appropriate, and provide the advantage of always having one visible; they can also be used in more extended configurations. The focus dependency on wavelength should then be tabulated, and regularly checked.

10 Phase

When applying phase calibration, we wish to minimize the calibration time, specially for fast phase switching. We wish to obtain a given **pathlength** accuracy in this mea-

surement. For each antenna, the pathlength precision obtained on a source is given by

$$\sigma_{\rm path} = \lambda \frac{\sigma_\phi}{2\pi} = \frac{c\sigma_0}{2\pi\nu S_\nu} = \frac{c\sigma_0}{2\pi S_{100}} \nu^{-1-\alpha} \tag{44}$$

With our standard units,

$$\sigma_{\rm path}(\mu{\rm m}) \simeq 500 \frac{\sigma_0}{S_{100}} \nu^{-1-\alpha} (t\Delta\nu)^{-1/2} \tag{45}$$

We have to use quasars as phase calibrators, since point sources are required. The typical spectral index of a quasar is -0.3 to -0.7. As for POINT and FOCUS, Figure 3 gives the optimal PHASE calibration frequencies as function of spectral index and observation conditions (percentiles). Taking the nearest quasar result in an expected flux $S_{100} = 0.1$ Jy for which

$$\sigma_{\rm path}(\mu{\rm m}) \simeq 70 (t\Delta\nu)^{-1/2} \tag{46}$$

The required pathlength accuracy is dependent on the observing frequency. The main goal is to minimize the coherence losses. The long term decorrelation loss is $\exp(-\sigma_\phi^2)$. A $\Psi = 3\,\%$ degradation in sensitivity (i.e. $\eta_p = 0.97$, consistent with our assumption of $\eta_c\eta_p = 0.85$ for a full 2-bit correlator) is obtained for $\sigma_\phi = 10^\circ$, corresponding to a path length of about 10 μm at 900 GHz. With 8 GHz bandwidth, this is reached in 6 seconds. The calibration time is

$$T_{\rm phase}({\rm sec}) \simeq 6 \left(\frac{\nu_{\rm obs}}{900{\rm GHz}}\right)^2 \frac{1}{\Psi} + {\rm slew\_time} \tag{47}$$

Eq.47 indicates the minimum integration time on a calibrator to determine the instrumental phase with 10° accuracy. However, the net remaining phase noise after a calibration cycle is given by the root phase structure function measured on an effective baseline length $b = vt_{\rm cycle}/2 + \theta L$ where L is the altitude of the turbulent layer above the site, θ the angular distance between the source and the calibrator, v the wind speed and $t_{\rm cycle}$ the cycle time. An optimal cycle is obtained when $vt_{\rm cycle} = 2\theta L$, which is 8 seconds for $L \simeq 1\,{\rm km}$, $\theta \simeq 2^\circ$, and $v \simeq 10\,{\rm m/s}$. However, the net phase error correspond to the root phase structure function on the effective baseline length b which is about 70 m in this case, giving a median pathlength $P(b) = 250\,\mu{\rm m}\,(b/300\,{\rm m})$, or $70 - 100\,\mu$m on such an effective baseline. Variations by a factor two in each direction will occur due to the weather statistics.

Phase errors will thus be completely dominated by atmospheric effects in the Fast Switching technique. The integration time on the calibrator can be decreased accordingly. With such short timescales, and balanced integration time between the source and the calibrator, decorrelation on source and on calibrator is similar, so that accurate amplitude calibration is still possible.

An alternate phase calibration technique is to use the Water Vapor Radiometer (WVR). In this case, the remaining phase error on medium timescales (longer than the fast cycle time $t_{\rm cycle}$, but shorter than the WVR stability time) is a combination of the WVR stability (expected to be 20 μm) and a fraction of the required pathlength

correction, $\epsilon P(vt)$. For calibration every minute or so, and $\epsilon = 0.1$ (10 % precision of the radiometer), the latter term is of order 30 μm. This assumes that this systematic error is antenna dependent, which is a worst case assumption valid for long baselines. Correlated errors will reduce this value to a baseline length dependent result.

A variant of the WVR calibration system is an empirical correction based on the correlation between WVR output and measured antenna phase. In 1 sec of time, which corresponds to the crossing time of the phase screen over one antenna diameter, the pathlength can be measured to about 20 μm precision, similar to the WVR stability. The correlation between WVR output and antenna phase could thus be empirically calibrated and regularly monitored by looking at the nearest quasar. Since the typical atmospheric timescale is 1 second, the correlation coefficient between WVR and measured phase would need 100 seconds to be measured with 10 % accuracy. This result is independent of the strength of the reference quasar.

The effect on images of the WVR phase correction are more subtle than in the fast switching case, since part of the remaining phase error still depend on baseline length. It will result in a pseudo-seeing, in which part of the source flux is scattered in an error beam, similar to adaptive optics at visible wavelengths with Strehl ratios of order 0.7 to 0.85.

11 Flux Scale

11.1 Ab-initio or "a posteriori" Amplitude Calibration ?

In the amplitude calibration, two somewhat different strategies exist.

"a posteriori" approach

The traditional approach used in current mm interferometers is to refer the amplitude scale to one (or more) reference quasars. This is an "a posteriori" scheme which offers the advantage of calibrating even poorly understood effects: the global system gain is measured in one operation by comparing the (non-calibrated) array output to the (assumed) source flux. To work efficiently, the integration time needed to reach the specified accuracy level must remain short compared to the available observing time. The integration time is given by

$$t_{\rm amp} = \left(\frac{100\sigma_0(\nu)}{S_0 \nu^\alpha} \right)^2 \frac{1}{\Gamma^2} \frac{1}{\Delta\nu} \tag{48}$$

Since the accuracy of opacity correction allows to take a source 10° away, we can use a Q_7 quasar of typical flux $S_0 = 1.5$ Jy, and $\Delta\nu = 8$ GHz, we obtain

$$t_{\rm amp}({\rm sec}) \simeq \left(\frac{\sigma_0}{30{\rm mJy}} \right)^2 \nu^{-2\alpha} \frac{1}{\Gamma^2} \tag{49}$$

For $\Gamma = 1\%$, taking the value of σ_0 from Fig.2, we find this is below 6 sec up to 350 GHz, but goes up to 10 minutes at submm wavelengths.

ALMA can certainly apply this scheme at low frequencies since the integration time to reach $\Gamma\,\%$ precision on the antenna gain is short. Short timescale guarantees negligible decorrelation losses. The differential opacity correction due to inaccurate opacity prediction will also be small for a 7° offset (see Section 6). Elevation dependent antenna gain plays a different role for small and extended sources.

The amplitude calibrator flux can be bootstrapped to a primary calibrator once during the observation. Some caution should be taken to match the elevation of the two calibrators during this process to within the required $10 - 15^\circ$ tolerance.

"ab-initio" method

At high frequencies, the above method is no longer valid, because the integration time becomes prohibitive. Limiting the calibration time to about 1 minute implies reducing the accuracy to about $\Gamma = 3\,\%$. For such integration times, the decorrelation effect is not completely negligible. The alternative method is to guarantee that the instrumental gain is stable and known with sufficient accuracy. This is an ab-initio absolute amplitude calibration. Since accurate control of the pointing and focus is possible within reasonable integration times, such a method can be applied to ALMA. This approach leaves two potential error terms:

- Imprecise receiver and atmospheric calibration
- Decorrelation effects

The first term affects the **relative** antenna calibration, and could potentially limit the imaging quality. Poor estimation of the second term could lead to incorrect absolute flux scale. The advantage of this method is that, in principle, when focus and pointing is well controlled, the antenna gain can be computed from the antenna characteristics (geometry, illumination, surface error). This prediction should be accurate enough at least at mm wavelengths, but perhaps not at submm wavelengths.

The effectiveness of "ab-inito" absolute calibration at high frequencies should be compared with that of the more classical "a posteriori" calibration.

Spectral Line case The above discussion on amplitude calibration was valid for continuum sources only. For spectral lines, the receiver sideband gain ratio becomes a dominant problem in the determination of the absolute flux scale. We have seen that this is a serious issue at submm wavelengths.

An hybrid approach In either scheme, receiver and atmospheric calibration is the critical issue. If this calibration step is unbiased, the averaging effect over the 64 antennas would probably allow to use the mean "ab-initio" flux determined from known antenna gains as an absolute measurement. Detailed studies of the biases of the atmospheric calibration step should thus be performed.

The only difference between the two approaches is the need, in the "a-posteriori" approach, to observe at the observing frequency a nearby quasar for (relative) flux calibration, and to bootstrap the flux of this amplitude calibrator to that of an "absolute"

calibrator. The later stage could potentially be omitted if one is confident in the lack of bias of the atmospheric calibration step.

Note that in the "a-posteriori" approach, the observation of amplitude calibrator can at very little cost be complemented by observations of the same calibrator at the calibration frequency, to measure the relative delay and phase between both receivers.

11.2 Absolute Flux Scale

While image quality depends on the **relative** calibration of the various antennas, which in turn is affected by the **antenna based** sensitivity, **absolute flux** calibration will depend on the **total array** sensitivity if standard "candles" are used.

In this respect, the huge (continuum) sensitivity of ALMA will be an asset to allow using so-called "absolute" calibrators as a flux scale reference. Rather than being confined to sources above 1 Jy or so like currently mm arrays, ALMA will be able to go down to much fainter sources, since the point source sensitivity is

$$\sigma_p = \frac{\sigma_b}{\sqrt{N(N-1)/2}} \simeq 2.0 - 3.5\mathrm{mJy} \left(\frac{T_{\mathrm{sys}}}{100\ \mathrm{K}}\right) \sqrt{\frac{1\ \mathrm{GHz}}{\Delta\nu} \frac{1\ \mathrm{sec}}{t}} \tag{50}$$

where the higher value accounts for the reduced antenna efficiency at submm wavelengths. Typical values are tabulated in Table 6. To reach the 1 % accuracy level, sources of order 10 mJy would be appropriate as primary amplitude calibrators in the mm range ($\nu < 250$ GHz), while sources of order 25-100 mJy would be required in the submm range ($\nu > 350$ GHz).

11.3 Integration time

The integration time necessary to reach this accuracy as function of the calibration source flux (Table 2 summarize the flux of sources described in Section 3) and ALMA sensitivity (Table 6) is given by :

$$t_p = \left(\frac{100}{\Gamma} \times \frac{\sigma_p}{S_\nu}\right)^2 \tag{51}$$

t_p is the point source integration time in second, Γ is the required accuracy (in percent), σ_p is the ALMA point source sensitivity with the full bandwidth (8 GHz) and S_ν is the source flux. The results of these computations at several frequencies are shown in Table 7.

For the secondary calibrators sources (e.g quasars) the required integration times can be extremely different. The strongest quasars used for RF bandpass calibration (called Q_{band} in Table 2) require very little time ($t \ll 1$ s). In the "a posteriori" method, amplitude calibration during the observing run is done with a quasar near the target source (quasars called Q_2,Q_4,Q_7 in Table 2). The elevation tolerance related to the opacity uncertainty allows the use of any of these quasars at mm wavelengths. The flux of these quasars can be measured very quickly (at most a few seconds). At sub-mm wavelengths, only Q_2 and Q_4 are acceptable for $\Gamma = 1\,\%$ accuracy, Q_7 is acceptable for

Table 7: Integration time (in seconds), for several frequencies and calibrators, needed with ALMA to achieve a relative flux precision $\Gamma = 1.0\,\%$. Computations were done based on Tables 2 and 6, and assume unresolved sources.

ν (GHz)	$Q_{\rm band}$	Q_2	Q_4	Q_7	*Star*	*Ast*	*Sat*
43.	< 0.01	.04	.002	.000	92000	284.0	.180
90.	< 0.01	.19	.007	.001	10000	32.0	.020
230.	< 0.01	3.1	.120	.014	1600	4.8	.003
350.	.01	16	.650	.070	1000	3.1	.002
410.	.01	47	1.900	.210	1300	4.1	.003
690.	.19	950	38.000	4.200	2000	6.1	.004
850.	.36	2000	79.000	8.800	1500	4.5	.003

$\Gamma = 3\,\%$, and the integration time to measured the flux with sufficient precision goes up to 1 minute.

Stars are too weak to be usable in any reasonable time ($t > 20$ min), unless the accuracy is relaxed to $3\,\%$. Asteroids would be fast to observe, but are poor absolute calibrators. Giant planet satellites provide the best compromise, with less than 1 second of integration time at any observing frequency to reach the required accuracy. Consequently, satellites are recommended for absolute flux calibration. However, size effects should be considered (see Section 11.4), and these satellites may not always be visible.

11.4 Resolved calibrator sources

Table 8: Synthesized beam (in arcsec) for several array configurations and frequencies. Configurations are from [Conway 2001].

ν (GHz)	sd	sc	sb	sa
43	3.74	1.84	0.81	0.41
90	1.79	0.87	0.39	0.20
230	0.70	0.34	0.15	0.08
350	0.46	0.22	0.10	0.05
410	0.39	0.19	0.08	0.04
690	0.23	0.11	0.05	0.03
850	0.19	0.09	0.04	0.02

Satellites (with size $\sim$ 1 arcsec) or larger source (planets) can be easily spatially resolved with ALMA, which means that the observed flux decrease with increasing baseline. Their use as primary calibrators thus requires a model fitting in the uv plane. Since

the flux decreases with increasing baseline, all the baselines do not contribute with the same weight to constrain the total source flux. Using a source model and the actual layout of the ALMA configurations, we can compute the effective noise on a $1''$ source from the baseline noise, and derive an "efficiency" as the ratio of the integration times required to get the same signal to noise on a $1''$ source and on a point source of same strength :

$$t_{\rm eff} = t_p/\varepsilon \tag{52}$$

ε can also be interpreted as the effective fraction of useful baselines. Table 9 gives this fraction of effective baselines (ε) as function of frequency and array configurations (the corresponding synthesized beams are indicated in Table 8). We used the configuration layout from ALMA memo 348 [Conway 2001]. The values allowing to reach a flux accuracy of 1% are shown in Table 10. In most cases, the integration time needed is still less than 1 second. Only at frequencies higher than 690 GHz and with a *sa* array configuration 10-20 seconds are required. The largest 14 km configuration has not been considered here. However, Table 9 shows that the effective number of baseline for configuration *sa* is only 1 at high frequencies. It is thus sufficient to design the largest configuration with 1 short baseline to provide the same sensitivity.

Table 9: Fraction (ε) of baselines constraining a 1 arcsec source (e.g. satellite) flux determination, for several array configurations and frequencies. The number of effective baselines can be obtained by multiplying by 2016.

ν (GHz)	sd	sc	sb	sa
43	0.90	0.88	0.57	0.23
90	0.82	0.63	0.23	0.068
230	0.48	0.21	0.051	0.014
350	0.28	0.10	0.024	0.0063
410	0.22	0.079	0.018	0.0046
690	0.092	0.028	0.0054	0.00055
850	0.063	0.019	0.0032	0.00016

12 Specific Methods

We have studied in the previous sections the different integration times for all calibration procedures, as function of the ALMA sensitivity, of the required flux accuracy (Γ) and of the calibrator fluxes. The integration time summary for each calibration step is presented in Table 11. Based on these integration times at each frequency, we propose in this section a specific method for each calibration step. Note that at low frequencies ($\nu \leq 410$ GHz), all the calibration procedures take less than 1 minute to be performed and are therefore not problematic. The main difficulty is to calibrate higher frequencies

Table 10: Integration time (in seconds) needed with ALMA to achieve an absolute amplitude accuracy of 1.0 % on a giant planet satellite of 1 arcsec angular size, for several frequencies and array configurations. Computations were done based on Tables 7 and 9

ν (GHz)	sd	sc	sb	sa
43	0.200	0.20	0.31	0.78
90	0.024	0.03	0.09	0.29
230	0.006	0.01	0.06	0.21
350	0.007	0.02	0.08	0.32
410	0.013	0.04	0.17	0.65
690	0.044	0.14	0.74	7.30
850	0.047	0.16	0.94	18.7

($\nu \geq 690$ GHz), because lower sensitivity and source fluxes both decrease the signal to noise compared to the low frequencies case.

12.1 Starting Observations

The first steps before observing is to tune the receiver, measure the sideband ratio, the delay and the RF bandpass. All these three procedures need to be done at the observing frequency (except the fine bandpass) with the strongest available quasars (called $Q_{\rm band}$ in Table 2). These quasars are, on average, 100 degrees away and telescopes take ~ 30 seconds to slew to this position. A pointing and focus (≈ 10 s, see below) is also required to optimize the signal to noise. One can now start these three first calibration steps. These starting procedures need altogether less than 1.5 minutes at low frequencies and between ≈ 4 minutes at higher frequencies. In fact, the most time expensive procedure at high frequency is the bandpass & sideband ratio measurement. If the subreflector coherent signal frequency dependence is known accurately enough, this step could be much faster.

12.2 Pointing and Focus

As indicated in Section 8, a short local pointing model every 30 minutes or so is better than measuring the pointing on a very nearby source. Focus will need to be measured every 10 to 30 minutes, depending on observing frequency, and on the success of a priori prediction.

12.3 Amplitude and Phase calibration

Phase calibration can be done either with fast switching, or using the WVR. In all cases, the integration time on the calibrator is not the limiting factor: residual atmospheric

Table 11: Integration times needed to reach Γ % Amplitude accuracy, 0.4″ Pointing accuracy, and the specified phase accuracy. The system frequency for each calibration step (F_{Cal}) is either ν_{Cal} (94 GHz) or the observing frequency ν_{Obs}. Phase is computed with S_{100}=0.1 Jy source (Q_2 2 degrees away source), and with S_{100}=0.5 Jy source (Q_4 4 degrees away source), Pointing, Focus and Amplitude (baseline and total) use a Q_4 source, while Bandpass uses a S_{100}=10 Jy source ($Q_{\rm band}$). At $\nu_{Obs} \leq 350$ GHz receivers are in SSB (10 dB), and at $\nu_{Obs} \geq 410$ GHz in DSB. Frequencies and bandwidths are in GHz, integration times in seconds.

	ν_{Obs} (GHz)		90	230	350	410	690	850	Precision
	Pwv (mm)		2.3	2.3	1.2	0.5	0.5	0.5	Goal &
	Precision Goal		$\Gamma = 1$ %			$\Gamma = 3$ %			Dependence
Procedure	F_{Cal}	$\Delta\nu$							
Unique Calibration Steps									
Delay	ν_{Obs}	8.0		< 0.03		0.09	1.7	3.4	$< 6°$
Sideband ratio	ν_{Obs}	0.250	0.2	2.5	11.7	4.4	87	170	$\propto 1/\Gamma^2$
Fine Bandpass (Amp)	ν_{Cal}	0.001	56	56	56	6.2	6.2	5.2	$\propto 1/\Gamma^2$
Fine Bandpass (Pha)	ν_{Cal}	0.001	0.75	0.75	0.75	0.75	0.75	0.75	5°
Large Bandpass (Amp)	ν_{Obs}	0.250	0.20	2.45	11.7	4.4	87	170	$\propto 1/\Gamma^2$
Large Bandpass (Pha)	ν_{Obs}	0.250	0.00	0.03	0.15	0.5	10	20	5°
Flux	ν_{Obs}	8.0		< 0.01		0.01	0.04	0.08	$\propto 1/\Gamma^2$
	Sum		60	60	70	12	100	190	$\propto 1/\Gamma^2$
Repetitive Calibration Steps									
Pointing	ν_{Cal}	16.0		$\simeq 60$			$\simeq 60$		0.4″
Focus	ν_{Cal}	16.0		$\simeq 8$			$\simeq 8$		$\propto 1/\Gamma$
Phase (Q_2 quasar)	ν_{Cal}	8.0	0.07	0.45	1.0	1.4	4.0	6	10°
Phase (Q_4 quasar)	ν_{Cal}	8.0		< 0.04			< 0.3		10°
Amplitude (on Q_4)	ν_{Obs}	8.0	0.9	11	53	20	390	750	$\propto 1/\Gamma^2$
Amplitude (on Q_7)	ν_{Obs}	8.0	0.10	1.2	5.9	2.2	44	85	$\propto 1/\Gamma^2$

effects will dominate. The relative phase (and delay) of the receiver at the observing and calibration frequencies should also be measured to guarantee accurate phase calibration.

Atmospheric transmission calibration (and receiver gain calibration) should be performed every 2–3 minutes, and differential opacity correction based on WVR sounding applied meanwhile. Relative amplitude calibration check is relatively easy at low frequencies, since it can be performed in less than 6 sec. However at high frequencies, this is no longer the case. We either have to relax the goal, or to rely on the "ab-initio" absolute calibration, based on pre-determined values of the antenna gain.

12.4 Absolute flux scale determination (Antenna gain measurement)

The simplest way to obtain a good absolute flux calibration, is to observe first a satellite (see Section 11) and after the amplitude calibration quasar Q_4 or Q_7. This is a standard

flux bootstrapping method. However, satellites are not always available, and they may not be at an elevation compatible with that of Q_4/Q_7. An ensemble of other secondary calibrators is thus required. Monitoring of these secondary calibrators should be done regularly to provide sufficient reference sources. Bandpass calibrators $Q_{\rm band}$ should be included in this monitoring, since they will always be observed at least once in a given project. From typical timescales of variations (0.15 % per day) this should be done at least once a week.

A variant is to use the satellite(s) to measure once the antenna gain, and rely later on the antenna gain to perform the temperature to flux conversion. This may be more accurate than the flux bootstrapping method, specially at high frequencies. However, because of limitation of the atmospheric transmission calibration, the expected accuracy does not exceed 2–3 %. [Pardo et al. 2001] report modeling the atmospheric transmission to about 1–2 % accuracy in the mm and submm range.

We have not yet addressed the problem of the first absolute antenna gain measurement. While a priori prediction from the laboratory measured receiver radiation pattern and known surface errors of the antenna may be sufficiently accurate at mm (3–1 mm) wavelengths, this is more challenging at submm wavelengths. Extrapolation using the spectral index knowledge from mm to submm wavelengths could be done. Reaching $\Gamma = 2\,\%$ at 650 GHz implies a knowledge of the spectral index to within 0.01 if the flux prediction is to be done from 100 GHz measurements.

Table 12: Typical observing cycle. $t_{\rm int}$ is the integration time per Procedure, in minutes or seconds. The repeat rate of each procedure is also indicated.

	$\nu < 400$ GHz		$\nu > 400$ GHz	
Accuracy	$\Gamma = 1\,\%$		$\Gamma = 3\,\%$	
Method	"a posteriori"		"ab initio"	
Procedure	$t_{\rm int}$	Repeat Rate	$t_{\rm int}$	Repeat Rate
Starting observation	~ 1 min	Once	~ 3 min	Once
Flux calibration	1 min	Once/Twice	2-10 min	Once/Twice
Pointing	~ 1 min	30–40 min	~ 1 min	15–30 min
Focus	8 sec	30-90 min	8 sec	10–30 min
Atmospheric calibration	3 sec	2–3 min	3 sec	2–3 min
Amplitude calibration	10 sec	2–3 min	1 min	10–30 min
Phase calibration	1 sec	20 sec	1 sec	5 sec
or with WVR	1 sec	2–3 min	1 sec	20 sec
Source observation	20 sec	20 sec	2-3 sec	5 sec
or with WVR	2 min	2 min	20 sec	20 sec

12.5 Observing cycle

In summary, we propose an observing cycle with two variants: Low and High frequencies. Integration time and rate of each procedure are indicated in Table 12. We have not

tried here to optimize the cycle time for the phase calibration, since this depends on the assumed technique (fast switching or WVR). The time losses associated to this problem actually dominates over all other calibration times.

13 Conclusions

We have studied in detail the different astronomical sources usable for calibration purpose. While some sources can be used without specific precaution for some purpose (e.g. pointing and focus in compact configurations), sources suitable for amplitude calibration need to match several criteria. This study shows that, together with **planets** as primary calibrators, **satellites** are good secondary flux calibrators. Special objects like **MWC 349** also have attractive properties and should be investigated. **Stars** and **asteroids** have inadequate properties (either too weak, or too variable or too polarized). No flux calibrator is yet known with sufficient accuracy. ALMA itself should be able to provide ab-initio measurements with 1% accuracy in the mm domain. Extrapolation at sub-mm wavelengths based on spectral index could yield 3 % accuracy. Very special purpose observations (e.g. simultaneous mm and near IR studies allowing more accurate spectral index measurements) may be required to improve that accuracy.

We have computed the ALMA integration time needed for all the calibration procedures, as function of the ALMA sensitivity, sources fluxes and required accuracy. The results of these computations indicate that:

- At high frequencies ($\nu \geq 690$ GHz), the *sideband ratio* calibration (and bandpass calibration) is the longest procedure (~ 30 minutes for 1 % accuracy, 3 minutes for 3 %), unless we can rely on a coherent signal injected at the subreflector.
- The short integration time (a few seconds) needed to measure the focus and pointing could allow "ab-initio" flux calibration, in which ALMA relies on prior knowledge of the antenna gains. To what accuracy can this antenna gain be predicted should be studied.
- The semi-transparent vane calibration system is less susceptible to errors induced by inaccurate atmospheric modeling than the dual-load system. Besides other arguments (see Memo 371 [Guilloteau & Moreno 2001]), this is another reason to favor such a system.
- Relative amplitude calibration at the 1 % level is feasible at mm wavelengths, but better than about 2–3 % will be difficult to obtain at submm wavelengths. The dominant problem here is the uncertainty in the atmospheric transmission, but the sensitivity conspires to limit independent checks using quasars to similar precision.
- Extrapolation of primary calibrator flux based on spectral index knowledge also results in a $\simeq 3$ % uncertainty at submm wavelengths. Hence, flux bootstrapping techniques will also be limited at this level.

The present document clearly indicates several directions which should be further developed to attempt reaching the highest possible calibration accuracy:

- Development of the vane calibration system, and in particular detailed study of its frequency dependence based on a prototype.
- Control of the receiver saturation properties. Saturation is (with sideband gain ratio) the most critical problem at mm wavelengths, and the driving consideration for the calibration device. Limiting it as much as possible will improve amplitude calibration in the mm domain.
- Development of the coherent signal in the subreflector for bandpass calibration. Note that such a signal could also be used to calibrate the vane transmission.
- Development of an accurate modeling of the antenna gain. Ab-initio prediction of the antenna gain from holography, beam pattern measurements, and ruze efficiency estimates would be an extremely valuable contribution to an accurate submillimeter calibration
- Modeling and measurement of the FIR filter response of the correlator. Accurate predictions of this behaviour would remove the need for fine bandpass calibration.
- Development of an atmospheric temperature monitoring device, since at submm wavelengths the calibration mostly depend on J_{m}.
- and of course, development of atmospheric modeling. Recent results [Pardo et al. 2001] in this area clearly indicate that the revised goals (1 % at mm wavelengths, 3 % at submm wavelengths) are indeed within reach. A detailed study of the possible biases would be helpful.

References

[Altenhoff et al 1994]
Altenhoff, W., Thum, C., Wendker, H.J., 1994
Radio emission from stars: a survey at 250 GHz.
Astron. and Astrophys. **281**, 161-183

[Bloom et al. 1999]
Bloom, S.T., Marscher, A.P., Moore, E.M., Gear, W., Teräsranta, H., Valtaoja, E., Aller, H.D. and Aller, M.F. (1999)
Multiwaveband observations of quasars with flat radio spectrum and strong millimeter–wave emission. *Astrophys. J. supp. ser.* **122**, 1-27.

[Bock et al. 1998]
Bock, D., Welch, W.J., Fleming, M. & Thornton D., 1998
Radiometric Calibration at the Cassegrain Secondary Mirror
ALMA memo 225

[Conway 2001]
Conway, J. 2001
A Preliminary ALMA Zoom Array Design for the Chajnantor Site.
ALMA memo 348

[de Pater and Massie 1985]
de Pater, I., Massie, S. T. (1985)
Models of the millimeter-centimeter spectra of the giant planets
Icarus **62**, 143-171.

[Guilloteau & Moreno 2001]
Guilloteau, S. and Moreno, R. (2001)
Receiver calibration scheme for ALMA.
ALMA memo 371

[Gurwell 1995]
Gurwell, M. A. 1995.
Planetary Atmospheres: Probing Structures Through Millimeterwave Observations of Carbon Monoxide
PhD thesis, California Institue of Technology, 1996.

[Hidayat 1997]
Hidayat, T. (1997)
Observations millimétrique et submillimétrique de Titan: Etude de la composition chimique et de son atmosphère. *Thèse de Doctorat de l'université Paris VII.*

[Lellouch et al. 1985]
Lellouch, E., Encrenaz, T., Combes, M. (1984)
The detectability of minor atmospheric species in the far infrared spectra of Jupiter

and Saturn
Astron. and Astrophys. **140**, 405-413.

[Lucas 1998]
Lucas, R. (1998)
Reference pointing of the ALMA antennas
ALMA Memo 189.

[Lucas 2000]
Lucas, R. (2000)
Reducing Atmospheric noise in single-dish observations with ALMA.
ALMA Memo 300.

[Mangum 2000]
Mangum, J. 2000
Amplitude Calibration at Millimeter and Sub-millimeter Wavelengths
ALMA Memo 318

[Moreno, 1998]
Moreno, R. (1998).
Observations millimétriques et submillimétriques des planètes géantes. Etude de Jupiter après la chute de la comète SL9.
Thèse de Doctorat. Université Paris VI.

[Moreno et al. , 2001]
Moreno, R., et al. 2001
Interferometric measurements of the Martian wind pattern, in prep.

[Mulheman and Berge 1991]
Mulheman, D.O., Berge, G.L. (1991)
Observations of Mars, Neptune, Io, Europa, Ganymede, and Callisto at a wavelength of 2.66 mm
Icarus **60**, 599-612.

[Neri et al. 1998]
Neri, R., Wink, J. and A. Patnaik (1998)
A survey of radio sources at 86 GHz.
IRAM working report.

[Ostro et al. 2000]
Ostro, S.J., Hudson, R.S., Nolan, M.C., Margot, J., Scheeres, D.J., Campbell, D.B., Magri, C., Giorgini, J.D. and Yeomans, D.K. (2000)
Radar Observations of Asteroid 216 Kleopatra.
Science **288**, 836–839.

[Pardo et al. 2001]
Pardo, J.R., Serabyn, E., and Cernicharo, J. (2001)

Submillimeter atmospheric transmission measurements on Mauna Kea during extremely dry El Nino conditions: implications for broadband opacity contributions
Journal of Quantitative Spectroscopy & Radiative Transfer, v. 68, iss. 4, p. 419-433.

[Paubert et al. 1984]
Paubert, G., Gautier, D., Courtin, R. (1984)
The millimeter spectrum of Titan - Detectability of HCN, HC3N, and CH3CN and the CO abundance
Icarus **60**, 599-612.

[Plambeck 2000]
Plambeck, R., 2000
Receiver Amplitude Calibration for ALMA
ALMA Memo 321

[Qian et al. 1991]
Qian, S.J., Quirrenbach, A., Witzel, A., Krichbaum, T.P., Hummel, C.A. and Zensus, J.A. (1991)
A model for the rapid radio variability in the quasar 0917+624.
Astron. Astrophys. **241**, 15-21.

[Redman et al. 1992]
Redman, R.O., Feldman, P.A., Matthews, H.E., Halliday, I. and Creutzberg, F. (1992).
Millimeter and submillimeter observations of the asteroid 4 Vesta.
Astron. J. **104**, 405-411.

[Redman et al. 1995]
Redman, R.O., Feldman, P.A., Pollanen, M.A., Balam, D.D. and Tatum, J.B (1995)
Flux density estimates at millimeter wavelength of asteroids near opposition from 1996 to 2005
Astron. J. **109**, 2869-2879.

[Redman et al. 1998]
Redman, R.O., Feldman, P.A. and Matthews H.E. (1998)
High-quality photometry of asteroids at millimeter and submillimeter wavelength
Astron. J. **116**, 1478-1490.

[Reid and Menten 1997]
Reid M.J. and K.M Menten (1997)
Radio photosphere of long–period variable stars.
Astrophys. J. **476**, 327-346.

[Rudy et al. 1987]
Rudy, D. J., Muhleman, D. O., Berge, G. L., Jakosky, B. M., Christensen, P. R. (1987).
Mars - VLA observations of the northern hemisphere and the north polar region at wavelengths of 2 and 6 cm.
Icarus **71**, 159-177.

[Rudy 1987]
Rudy, D.J. (1987)
Mars: High resolution VLA observations at wavelengths of 2 and 6 cm and derived properties.
Ph.D. Thesis California Inst. of Tech., Pasadena. 1987

[Steppe et al. 1993]
Steppe H, G.Paubert, H.P. Reuter, A. Greve, S.Liechti, B. LeFloch, W. Brunswig, C. Menéndez and S. Sanchez (1993)
Astron. & Astrophys. Suppl. Ser. **102**, 611-635.

[Ulich 1981]
Ulich, B.L. (1981)
Millimeter-wavelength continuum calibration sources.
Astron. J. **86**, 1619-1626.

[Ulich & Haas, 1976]
Ulich, R. & Haas, R.W., 1976
Amplitude Calibration of Millimeter Wavelengths Spectral Lines
ApJ Supp. 30, 247

[Yun et al. 1998]
Yun M.S., Mangum, J., Bastian, T., Holdaway, M., Welch, W.J., 1998
"Accurate Amplitude and flux calibration of the MMA"
MMA Memo 211.